

# JGR Solid Earth

## RESEARCH ARTICLE

10.1029/2020JB020158

### Key Points:

- A rotating pressure source determined by InSAR data indicates how crystal mush is pressurized
- Dilatancy in a pre-existing weak zone may open channels to allow for pore fluid injection to trigger volcano-tectonic earthquakes
- A water table drop due to dilatation in a pre-existing fault zone may have drained the crater lake at Korovin and triggered the phreatic eruption

### Supporting Information:

- Supporting Information S1

### Correspondence to:

Y. Zhan,  
[yzhan@carnegiescience.edu](mailto:yzhan@carnegiescience.edu)

### Citation:

Zhan, Y., Gregg, P. M., & Lu, Z. (2021). Modeling magma system evolution during 2006–2007 volcanic unrest of Atka volcanic center, Alaska. *Journal of Geophysical Research: Solid Earth*, 126, e2020JB020158. <https://doi.org/10.1029/2020JB020158>

Received 9 MAY 2020

Accepted 16 JAN 2021

## Modeling Magma System Evolution During 2006–2007 Volcanic Unrest of Atka Volcanic Center, Alaska

Yan Zhan<sup>1,2</sup> , Patricia M. Gregg<sup>1</sup> , and Zhong Lu<sup>3</sup> 

<sup>1</sup>Department of Geology, University of Illinois – Urbana-Champaign, Urbana, IL, USA, <sup>2</sup>Now at: Earth and Planets Laboratory, Carnegie Institution for Science, Washington, DC, USA, <sup>3</sup>Huffington Department of Earth Sciences, Southern Methodist University, Dallas, TX, USA

**Abstract** Surface deformation and seismicity provide critical information to understand the dynamics of volcanic unrest. During 2006–2007, >80 mm/yr uplift was observed by interferometric synthetic aperture radar (InSAR) at the central Atka volcanic center, Alaska, coinciding with an increasing seismicity rate. On November 25, 2006, a phreatic eruption occurred at the Korovin volcanic vent, 5-km north of the central Atka, following the drainage of its crater lake a month prior to the eruption. The InSAR data are assimilated into three-dimensional finite element models using the Ensemble Kalman Filter to investigate: (1) the pressure source creating the surface deformation; (2) the triggering of the volcano-tectonic (VT) earthquakes in the Atka volcanic center; and (3) the triggering of the phreatic eruption at Korovin. The models show that the pressure source required to create the surface deformation is a NE-tilted, oblate ellipsoid, which rotated from steep to gentle dipping from June to November 2006 before the eruption. The modeled dilatancy in a pre-existing weak zone, coinciding with the Amlia-Amukta fault, driven by the pressure source has a spatial and temporal correlation with the evolution of the VT earthquakes during the unrest. The fault dilatancy may have increased the connected porosity and permeability of the fault zone allowing fluid injection which triggered the observed seismicity. In addition, the dilatated fault may have increased the fluid capacity of the fault zone by  $\sim 10^5$  m<sup>3</sup>, causing the discharge of the crater lake at Korovin. Consequently, the phreatic eruption of the Korovin volcano may have been triggered.

## 1. Introduction

Volcanic unrest, when the behavior of a volcano deviates from its baseline or background (e.g., Acocella, 2014; Phillipson et al., 2013), may provide critical warnings for potential volcanic eruptions (e.g., Moran et al., 2011; Phillipson et al., 2013; Sparks, 2003). To determine whether and when an eruption will occur, it is critical to understand the mechanisms causing the volcanic unrest. Recent developments in volcanic monitoring by geodesy (e.g., InSAR and GNSS) and seismology (e.g., broadband seismometers) allow us to explore the host-rock responses to the changes in the physical conditions of a magmatic system (Sparks et al., 2012). In addition to observations, physical models enable us to test hypotheses proposed for explaining and forecasting volcanic unrests (e.g., Charco & Galán del Sastre, 2014; Currenti et al., 2007; Del Negro et al., 2009; Fournier & Chardot, 2012; Gerbault, 2012; Gregg et al., 2013; Grosfils, 2007; Hickey et al., 2015; Le Mével et al., 2016; Manconi et al., 2010; Masterlark, 2007; McTigue, 1987; Mogi, 1958; Segall, 2013; Yang et al., 1988; Zhan & Gregg, 2019).

Data assimilation techniques based on the Bayesian Markov chain Monte Carlo method allow us to utilize volcanic monitoring data to obtain probabilistic estimates of model parameters and forecast future behavior (e.g., Albright et al., 2019; Anderson & Segall, 2013; Bato et al., 2017; Gregg & Pettijohn, 2016; Segall, 2013; Zhan & Gregg, 2017). Combining surface deformation and seismicity data with advanced numerical models can provide critical insights into the mechanisms of the restless behaviors of a volcanic system prior to its eruption. In particular, the volcano-tectonic (VT) earthquakes triggered by brittle failure are generated by the evolution of stress field in the crust, which also produces an observable surface deformation. Due to crustal heterogeneity, hydrothermal systems, and other factors, the stress field controlling surface deformation and seismicity can vary from one system to another (Roman & Cashman, 2018).

The Atka volcanic center is located at the northeast end of Atka Island (Figure 1a), which is the largest modern magmatic complex in the central Aleutian arc, with an estimated eruptive volume of  $\sim 200$  km<sup>3</sup> since

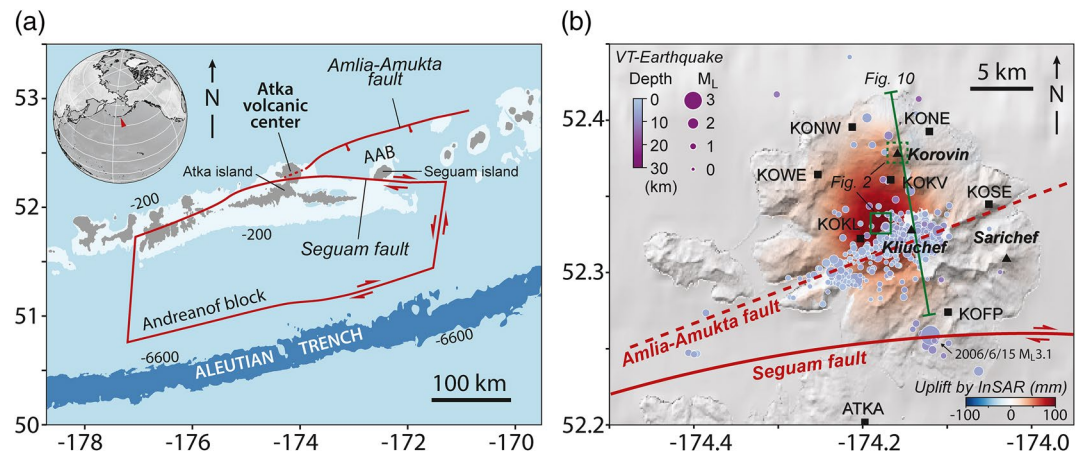


**Figure 1.** (a) The location of the Atka volcanic center (called Atka for simplification). Atka is located on an extended crust in the north of the Andreanof Block (after Geist et al., 1987; Singer et al., 1992). Atka is also at the junction of the Segum and AA faults. AAB -Amlia and Amukta intra-arc summit basins. (b) The surface uplift from 2000/7/1 to 2006/11/14 revealed by the InSAR data. VT earthquakes (Power et al., 2019) occurring between 2006/6/1 and 2007/1/1 are plotted as purple circles whose color and size represent depth and magnitude. The black squares are the locations of the seismometers (<https://avo.alaska.edu/>). The black triangles show the locations of some major volcanic vents at Atka. The solid red lines show the fault traces after Geist et al. (1987), and the red dashed line shows the possible trace of the AA fault indicated by the earthquake distribution and topography. The green line shows the location of the cross-section in Figure 10. The green boxes show the areas (solid line for the Atka center; dashed line for the Korovin volcano) to calculate the time series of displacement in Figure 2. AA, Amlia-Amukta; InSAR, interferometric synthetic aperture radar; VT, volcano-tectonic.

presumed Tertiary age (Myers et al., 2002). The Atka complex belongs to an extended crust to the north of the Andreanof Block (Geist et al., 1987; Singer et al., 1992). Two faults, the Amlia-Amukta (AA) fault and the Segum fault, cut the Atka volcanic center. The central part of the AA fault is a normal fault serving as the north boundary of the Amlia and Amukta intra-arc summit basins (Geist et al., 1987, Figure 1a). At Atka Island, a linear crustal structure, which may be a part of the AA fault, controls the distribution of the observed earthquakes (Power et al., 2019, Figure 1b). Interferometric synthetic aperture radar (InSAR) data suggests that there has been no observable motion of this segment of the fault in recent decades. However, we suggest that the AA fault in the Atka Island plays an important role as a pre-existing weak zone running through the Atka volcanic center. The Segum fault, to the south of AA and the Atka volcanic center, is thought to be a right-lateral strike-slip fault as the north boundary of the Andreanof Block (Geist et al., 1987). The youngest phase of volcanic activity in Atka began about 1–2 Myrs ago (Myers et al., 2002). The Atka volcano was once a large shield volcano, later destroyed due to a caldera collapse eruption 0.3–0.5 Myrs ago (Marsh, 1990). Subsequently, four major volcanic cones (Korovin, Kliuchef, Sarichef, and Konia) have formed around the Atka caldera through a series of complex magmatic processes, including melting, crystal fractionation, and magma mixing (Myers et al., 2002). The Korovin cone, the largest of the post-caldera edifices with a height of 1.5 km and basal diameter of 7 km, has erupted several times in the past 50 years (i.e., 1976, 1987, 1998, and 2006) and has been the location of numerous fumarolic and hydrothermal events during the past 200 years (Lu & Dzurisin, 2014).

During 2006/6–2007/1, uplift at a rate  $>80$  mm/yr was observed in the center of the Atka volcanic center (Figure 1a) by InSAR (Lu & Dzurisin, 2014), coinciding with an increased seismicity rate near the center of deformation (Power et al., 2019, Figures 1b and 2). Simultaneously, increased fumarolic and hydrothermal activity occurred at Korovin volcano, located 5-km north to the center of uplift. The unrest at Korovin was followed by a lake drainage event at the crater of Korovin prior to October 19, 2006 (Neal et al., 2008, Figure 2). On November 25, 2006, an eruption (VEI 1; <https://volcano.si.edu/>) occurred from Korovin. Although the satellite images show a small amount of ash deposited near the Korovin vent, they are likely to be remobilized ash dislodged during a phreatic eruption (Neal et al., 2008).

This study focuses on the unrest observed at Atka volcano because: (1)  $\sim 50,000$  passengers fly over the Aleutian Arc each day and active volcanoes in this region pose a significant aviation risk (<https://www.usgs.gov>).

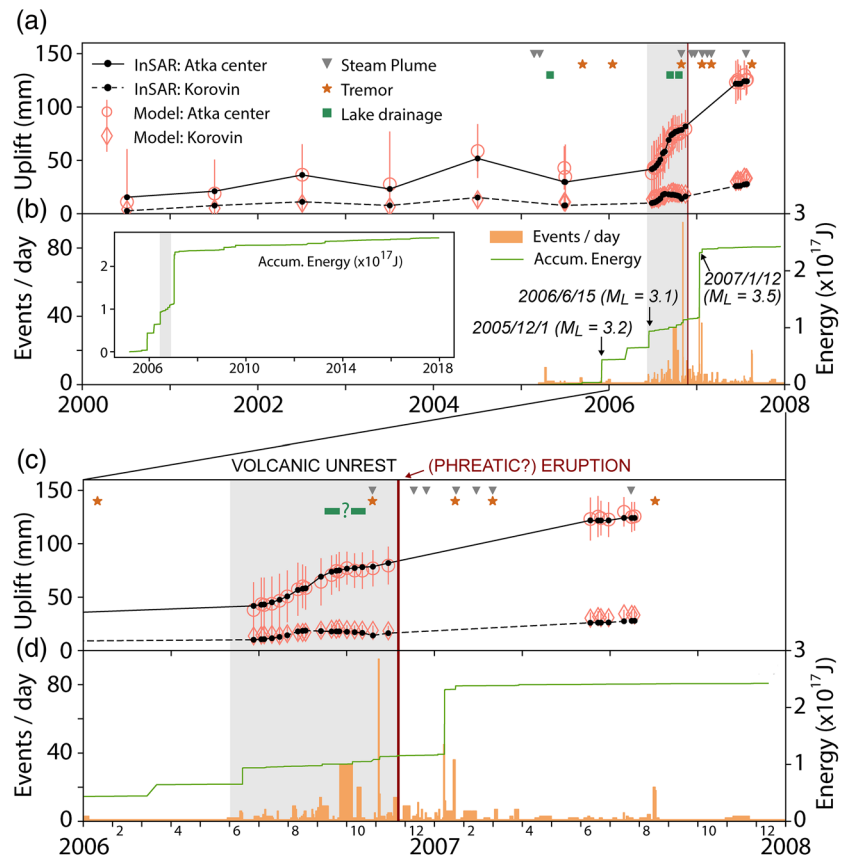


**Figure 2.** The time series of ground deformation and VT earthquakes from 2000 to 2008. (a) Surface uplift at Atka center and Korovin (Figure 1b) revealed by InSAR data are shown as the black solid and dashed lines. Each black circle represents one InSAR time slice. The red circles and diamonds are the surface deformation calculated by the numerical models (i.e., Model II) with data assimilation. The unrest events, including steam plumes, tremors, and lake drainage are labeled as gray triangles, orange stars, and green boxes (McGimsey et al., 2007, 2011; Neal et al., 2008). (b) The numbers of VT earthquakes per day are shown as orange bars. The green line is the accumulated energy calculated by  $\log_{10}(\text{Energy}) = 11.8 + 1.5 M$  (Gutenberg, 1956). The inserted plot in the panel (b) shows the accumulated energy from 2005 to 2018. (c) and (d) show the ground deformation and VT earthquakes from 2006 to 2008. The gray shadows highlight the volcanic unrest. The thick red lines illustrate the phreatic eruption. InSAR, interferometric synthetic aperture radar; VT, volcano-tectonic.

gov/media/images/air-traffic-over-active-volcanoes-aleutians); (2) Korovin Volcano at the rim of the Atka remains active today; and (3) InSAR and seismic data provide an excellent coverage of the 2006 eruption and subsequent activity, allowing us to study the relationship between deformation and seismicity. In particular, the key puzzle of the 2006–2007 volcanic unrest is whether the restless behavior occurring at central Atka triggered the phreatic eruption at Korovin, 5-km away. A large offset ( $>5$  km) between the deformation center and its nearest eruptive vent is not rare in the nature (Ebmeier et al., 2018), and some of the eruptions are associated with the interaction between magmatism and local fault systems, such as the Sabancaya volcano (MacQueen et al., 2020). Therefore, the Atka Volcanic Center provides an example to study the interaction between magma reservoirs, pre-existing fault zones, and hydrothermal systems.

In this study, a series of three-dimensional finite element models are developed to simulate the surface deformation revealed by multi-temporal InSAR data from July 1999 to July 2007. The probabilistic estimation of the pressure source evolution is obtained using the Ensemble Kalman Filter data assimilation technique. The stress, strain, and failure of the crust are calculated to explore the interaction between the pressurized source and two pre-existing weak zones (i.e., Amlia-Amukta fault and Seguam fault). The model infers that the fracturing and hydrous processes of the pre-existing fault zone can explain the spatial and temporal evolution of the volcano-tectonic (VT) earthquakes during the unrest. After combining the model

results and multiple observations, the study suggests that the 2006/11/25 phreatic eruption of the Korovin volcano is triggered by the restless behavior at the central Atka.

## 2. Pressure Source Evolution

### 2.1. InSAR Data

We generated InSAR images acquired by ERS-2 and Envisat satellites between mid-June and late October during 1997–2007 to ensure the InSAR coherence. The coherence can be easily lost due to seasonal snow and ice cover but maintained during or between summers (Lu & Dzurisin, 2014). Data from 5 ERS-2 tracks and 5 Envisat tracks were used in this study (Table S1). SAR data from each of the 10 tracks were processed separately to form interferograms using images from the same track by the same sensor. ERS-2 and Envisat images of the same day were separated by ~30 min apart. Due to a small discrepancy in wavelength (5.66 cm and 5.63 cm for ERS-2 and Envisat, respectively), ERS-2 and Envisat images cannot be paired to generate coherent interferograms unless the spatial baseline is about ~2 km and the imaging area is relatively flat (e.g., Lu et al., 2012). So, ERS-2 and Envisat images of the same track were processed independently to form the interferograms to study the volcanic deformation at Atka. Interferograms with low coherence and severe atmospheric artifacts were removed through visual inspection and the pairwise logic method (e.g., Lu et al., 2000; Massonnet & Feigl, 1995). A standard ERS-2/Envisat frame can cover more than 35 km latitude wise on the eastern part of the Atka Island (Figure 1). As the Atka volcanic center, including the Korovin volcano, only occupies the northeastern portion of the island, atmospheric artifacts on the southern parts of the island provide guidance on interferogram selection. Detailed information about the image acquisition dates and LOS geometries of 73 interferograms used in the deformation time-series analysis is shown in Table S1.

As interferograms were from a combination of tracks of different line-of-sight (LOS) imaging geometries (Table S1), we applied a multiple-InSAR small baseline subset (MSBAS) technique (Kim & Lu, 2018; S. Samsonov et al., 2013) to obtain the time series of surface displacements in the vertical and east-west components (Tables S1 and S2). The MSBAS is a simple extension of the standard SBAS (e.g., Berardino et al., 2002; Hooper, 2008) for estimating two-dimensional time-series deformation based on multitemporal InSAR images. The strength of the MSBAS is its capability of combining InSAR datasets from different wavelength (e.g., L-, C- and X-band) and geometries (e.g., ascending, descending) because the LOS imaging parameters (azimuth and incidence angles) and radar wavelengths are included to the equation governing the observed interferograms phase and the components of deformation vector (Kim & Lu, 2018; S. Samsonov et al., 2013). The technique has been widely used for the automatic generation of standard and advanced deformation products from RADARSAT Constellation Mission SAR data by the Canada Center for Mapping and Earth Observation (S. Samsonov, 2018).

In this study, all interferograms were filtered and unwrapped. Atka Island is not monitored with any in-situ geodetic instruments. The inspection of all interferograms of Korovin (Lu & Dzurisin, 2014) indicates the far-field deformation over the northernmost and easternmost edges of the island is negligible. So, we select the northernmost edge of the Atka Island as the reference area with zero deformation. To exclude the effect of reference selection on deformation pattern, we have also tested a zero-phase reference over the easternmost edge of the island. It produces nearly identical results. The unwrapped phases were then geocoded to the same map coordinate. The governing equation for calculating the vertical and east-west components of time-series deformation rates from interferograms of multiple LOS geometries is:

$$\begin{pmatrix} -\frac{4\pi}{\lambda_i} \cos \alpha_i \sin \beta_i S_i & \frac{4\pi}{\lambda_i} \cos \beta_i S_i & -\frac{4\pi}{\lambda_i} \frac{1}{R_i \sin \beta_i} B_i \\ 0 & L & 0 \end{pmatrix} \begin{pmatrix} V_E \\ V_V \\ \Delta h \end{pmatrix} = \begin{pmatrix} \Phi_i \\ 0 \end{pmatrix} \quad (1)$$

where  $R_i$ ,  $\alpha_i$ , and  $\beta_i$  are the slant range distance from the satellite to the target, the azimuth angle of the satellite track, and the incidence angle at the target in the  $i^{th}$  interferogram.  $\lambda_i$  is the SAR wavelength.  $S_i$  is a matrix constructed from time intervals of consecutive SAR acquisitions of all tracks spanned by the  $i^{th}$  inter-



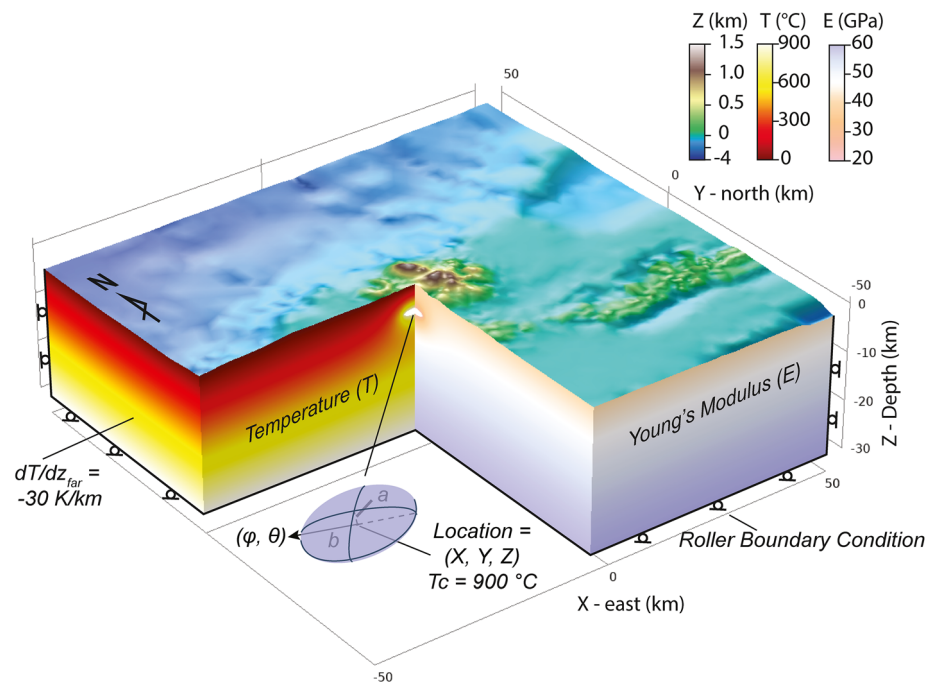


**Figure 3.** The temperature and Young's modulus of the numerical model. The pressure source for the ground deformation during the volcanic unrest is modeled by an oblate ellipsoid. The center of the ellipsoid is at  $(X, Y, Z)$ . The half-height and half-width of the ellipsoid are  $a$  and  $b$ . The dipping angle (plunge) and azimuth (from North) of the half-width ( $b$  axis) are  $\theta$  and  $\phi$ . The bottom and lateral surfaces are defined as the roller-type boundary condition.

ferogram.  $L$ , a Tikhonov matrix used for ill-posed problems in case of rank deficiency of a design matrix, is composed of a regularization parameter and a zero-, first-, or second-order difference operator (Samsonov & d'Oreye, 2017).  $V_V$  and  $V_E$  are the vertical and the east-west components of the deformation rate vector during consecutive SAR acquisitions.  $B_i$  is the perpendicular baseline of the  $i^{th}$  interferogram.  $\Delta h$  is the topography error.  $\Phi_i$  is the observed phase of the  $i^{th}$  interferogram (Kim & Lu, 2018; S. Samsonov et al., 2013). The unknown parameters of the deformation rates ( $V_V$  and  $V_E$ ) between two adjacent SAR images of the entire interferogram stack were calculated by solving the Equation 1 via singular value decomposition with minimum-norm constraints, which is a typical protocol used to solve under-ranked equations (S. Samsonov et al., 2013; Samsonov & d'Oreye, 2017). Time-series of ground displacement (i.e., the cumulative deformation in the vertical and east-west components) were reconstructed by integration. Finally, each image in the time series was further down sampled to about 2,500 data points by the quadtree partitioning (e.g., Zhan et al., 2019).

## 2.2. Numerical Model of the Atka Volcanic System

The setup of the numerical model of the Atka volcanic system is similar to the previous study in the Laguna del Maule volcano (Zhan et al., 2019). The finite element models are built and solved using COMSOL Multiphysics 5.3a, which has been well benchmarked with analytical solutions (e.g., Gregg et al., 2012; Zhan & Gregg, 2017).

The study area is modeled as a  $100 \times 100 \times 30$  km box (Figure 3) centered at the central Atka Island ( $51.331^\circ\text{N}$ ,  $174.139^\circ\text{W}$ ). The Global Multi-Resolution Topography Data (Ryan et al., 2009) is used to build the surface elevation of the model. A pressurized spheroid within the box is used to create the surface deformation at the center of the Atka Island. The geometry of the spheroid is defined by its location ( $X$ ,  $Y$ , and  $Z$ ), half-height ( $a$ ), half-width ( $b$ ), plunge of  $b$  axis ( $\theta$ ), and azimuth of  $b$  axis ( $\phi$ ; Figure 3), which is similar to Yang et al. (1988)'s ellipsoid analytical model. For example, if the pressure source is a sill like a horizontal pancake, the half-width ( $b$ ) should be much larger than the half-height ( $a$ ), and the plunge of  $b$

( $\theta$ ) should be zero. The bottom and lateral edges of the crustal model are defined as a roller-type boundary condition. A two-step loading is applied to the model. First, the model is loaded by a gravitational body force and a surface water pressure ( $\rho_w g h_w$ ) to calculate the initial stress. The initial stress is deviating from the lithostatic stress near the surface with topography (McTigue & Mei, 1981). Second, a pressure excess to the initial pressure along the boundary of the ellipsoid is loaded, named as overpressure ( $OP$ ). The deformation during the second step represents the response of the host-rock to the pressure source, which is used in the data assimilation with the InSAR data.

The linear elastic model has a spatial variation in Young's modulus ( $E_d$ ) and a constant Poisson's ratio ( $\nu$ ), since Poisson's ratio has much less impact on the model results than Young's modulus (Zhan & Gregg, 2019). Similar to Zhan et al. (2019), Young's modulus of the model is a function of both depth and temperature, which is defined by

$$E_{Td} = \beta_T E_d, \quad (2)$$

where  $E_d$  is the far-field Young's modulus, which is not affected by the heated magma reservoir. The far-field Young's modulus,  $E_d$ , is defined by

$$E_d = -0.0125 z^2 - 1.25 z + 40.25, \quad (3)$$

which is consistent to the seismic velocity profiles in the adjacent area (Flidner & Klemperer, 1999), considering the relationship between dynamic and static Young's modulus (Ciccotti & Mulargia, 2004; Starzec, 1999; Figure S3). The constants and variables in the equations are listed in Tables S2 and S3.

In Equation 2,  $\beta_T$  is a temperature-controlled coefficient defined as

$$\beta_T = \frac{1}{2 - 2e} \left[ \exp\left(\frac{T - T_d}{T_c - T_d}\right) + 1 - 2e \right], \quad (4)$$

where  $T_d = z dT / dz$ , the geothermal gradient,  $dT / dz$  is 30°C/km (Currie & Hyndman, 2006), and  $e$  is he base of the natural logarithm. The temperature of the magma reservoir,  $T_c$ , is 850°C, considering a silicic crystal mush may underlay the center of Atka (Myers et al., 2002). This equation defines a 50% decrease in the Young's modulus of silicic rocks when the temperature approaches its solidus (after Figure 3b in Smith et al., 2009). For example, when the temperate equals geothermal temperature,  $T_d$ , the coefficient ( $\beta_T$ ) is one. When the temperate is  $T_c$ , the coefficient ( $\beta_T$ ) is 0.5. The temperature is calculated using a steady-state heat conduction model with the same geometry and mesh (e.g., Zhan et al., 2019).

### 2.3. Model Parameter Estimation by Ensemble Kalman Filter

The pressure source generating the ground deformation is determined by the Ensemble Kalman Filter (EnKF) workflow for volcanoes as the previous studies (e.g., Zhan & Gregg, 2017). The EnKF analysis updates the model states by solving the Bayesian problem using a Monte Carlo method (Evensen, 2003). A matrix containing all the model parameters and results can be updated by:

$$\mathbf{A}_{i+1} = \mathbf{A}_i + \mathbf{X}_i \mathbf{H}^T \left( \mathbf{H} \mathbf{X}_i \mathbf{H}^T + \mathbf{R}_i \right)^{-1} (\mathbf{M}_i - \mathbf{H} \mathbf{A}_i), \quad (5)$$

where  $\mathbf{A}_{i+1}$  is updated ensemble by the EnKF analysis,  $\mathbf{A}_i$  is a forecasting ensemble by the numerical models,  $\mathbf{X}_i$  is the covariance matrix of  $\mathbf{A}_i$ ,  $\mathbf{M}_i$  is perturbed measurements (by adding 10% white noise) whose covariance matrix is  $\mathbf{R}_i$ , and  $\mathbf{H}$  is the coordinating matrix (Evensen, 2003). In this study, the results from the numerical models are the East-West and Up-Down components of surface displacement (Figure 4), which will be assimilated in each step when the corresponding InSAR time series data is available. The parameters solved by the EnKF analysis are the geometric parameters of the pressure source ( $X$ ,  $Y$ ,  $Z$ ,  $a$ ,  $b$ ,  $\theta$ ,  $\phi$ ), and the overpressure ( $OP$ ; Figure 5). The number of ensemble members (i.e., numerical models) and intrastep iterations are set as 100 and 5 to reach maximum efficiency.

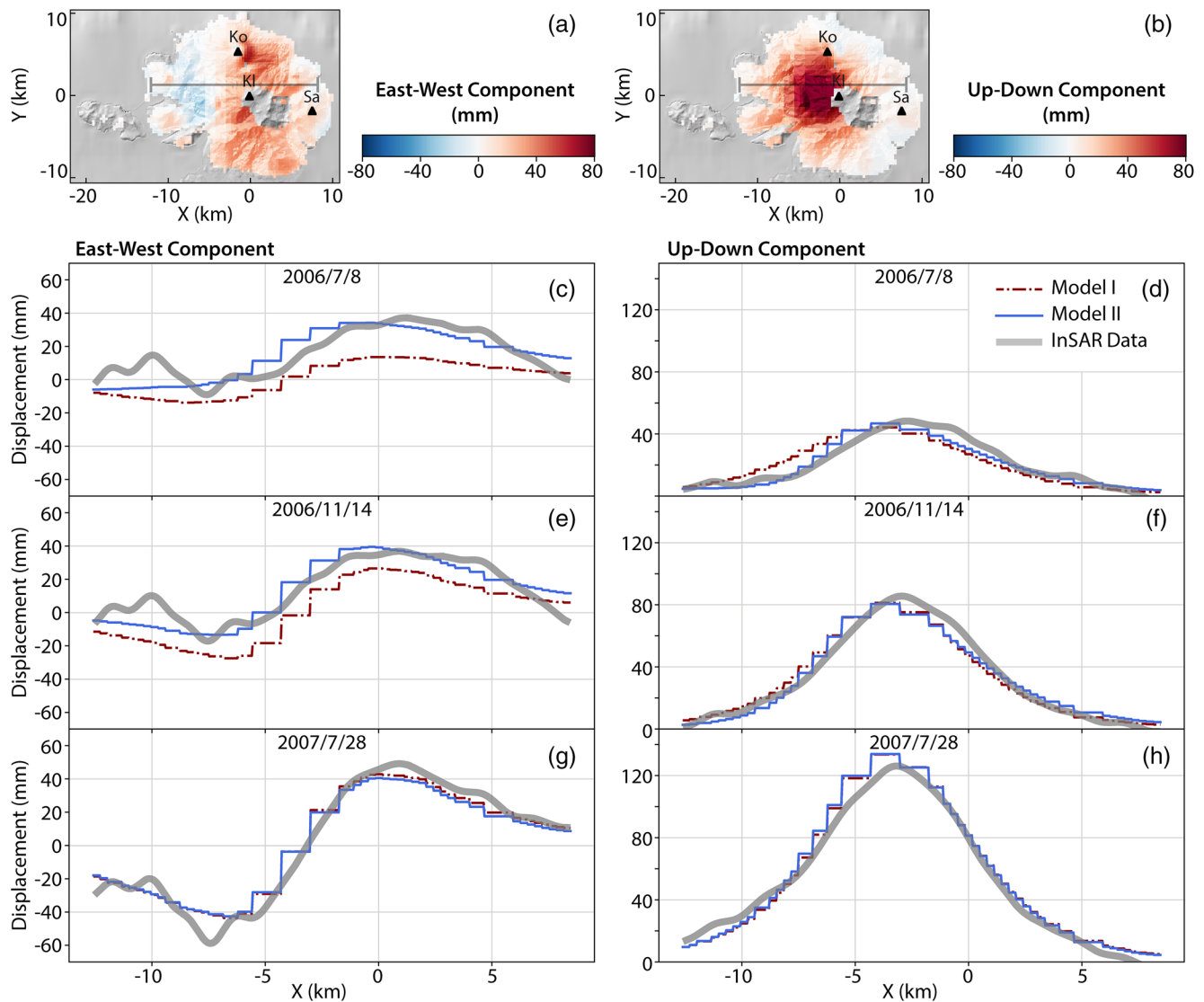


**Figure 4.** Comparison between InSAR time series data and modeled surface displacement. (a) and (b) are the East-West and Up-Down displacements from 2000/7/1 to 2006/11/14 by the down sampled InSAR data. The black triangles represent the volcanos: Korovin (Ko), Kliuchef (Kl), and Sarichef (Sa). The gray lines show the cross-sections in figures (c)–(h). (c)–(h) show the cross-sections of the InSAR data and the modeled displacement. In Model I (red dash-dot lines), the pressure source is an ellipsoid with a fixed dipping angle ( $\theta = 0^\circ$  in Figure 3). In Model II (solid blue lines), the dipping angle ( $\theta$ ) and azimuth (from North;  $\phi$ ) are unfixed. The gray, thick lines are the InSAR data. InSAR, interferometric synthetic aperture radar.

In this study, two EnKF tests are conducted with two different model settings. In Model I, the pressure source is an ellipsoid with a fixed, upright “a” axis ( $\theta = 0^\circ$  in Figure 3). In Model II, the ellipsoid is allowed to rotate freely.

#### 2.4. Volcanic Deformation and Pressure Source

The InSAR data shows the surface deformation at the Atka center accelerated from  $\sim 5$  mm/yr to  $\sim 80$  mm/yr in June 2006 when the volcanic unrest started (Figure 2a and 2c). Then, the uplift rate at the center dropped to  $\sim 10$  mm/yr in September 2006 until the 2006/11/25 eruption (Figure 2c). There was an uplift of  $\sim 40$  mm occurring at the Atka center within 6 months after the eruption (Figure 2c). After that, the rate of uplift was back to the background ( $< 5$  mm/yr). However, the temporal variation in surface deformation from 2006/11/14 to 2007/6/12 was not captured due to the lack of coherent InSAR acquisitions.

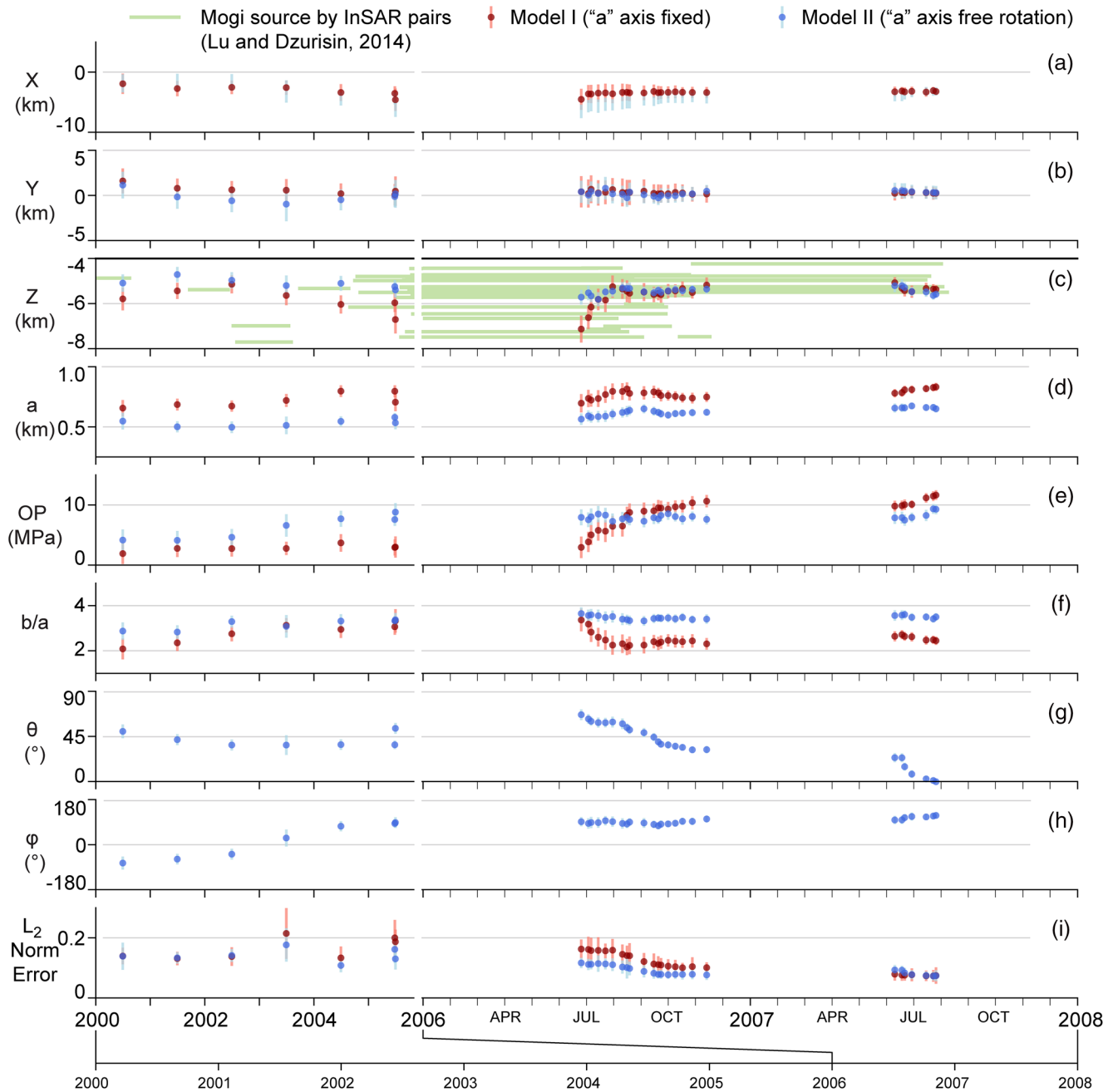


**Figure 5.** Evolution of the parameter estimations by the EnKF. The parameter estimation of the pressure source for each InSAR acquisition includes (a) X-location, (b) Y-location, (c) Z-location, (d) half-height,  $a$ , (e) overpressure,  $OP$ , (f) ratio between half-width and half-height,  $b/a$ , (g) plunge of half-width axis,  $\theta$ , and (h) azimuth (from North) of the  $b$  axis,  $\phi$ . (i) The  $L_2$  norm error of surface displacement (e.g., Zhan et al., 2017) shows the overall misfit between models and data. The colored circles are the mean values of the ensemble members, and the bars are two times of the standard deviation indicating a  $\sim 95\%$  confidence interval. Red error-bar plots show the results of Model I with an upright “ $a$ ” axis ( $\theta = 0^\circ$  in Figure 3). Blue shows the results of Model II with a freely rotating ellipsoid. Green lines show the depth of the Mogi sources inverted by the InSAR pairs by the previous study (Lu & Dzurisin, 2014). EnKF, Ensemble Kalman Filter; InSAR, interferometric synthetic aperture radar.

The uplifting center is located  $\sim 3$ -km west of Kliuchef near the central Atka (Figures 4 and S4). An uplift of  $\sim 40$  mm was observed during the 6-month time interval immediately before the eruption (Figure 4d). Meanwhile, the East-West component of displacement slightly changed (Figure 4c and 4e). However, during the 8-month interval after the eruption (2006/11/14–2007/7/28), a 40-mm west-warding, a 20-mm east-warding, and a 40-mm up-warding displacement were observed (Figure 4g and 4h). The change of the



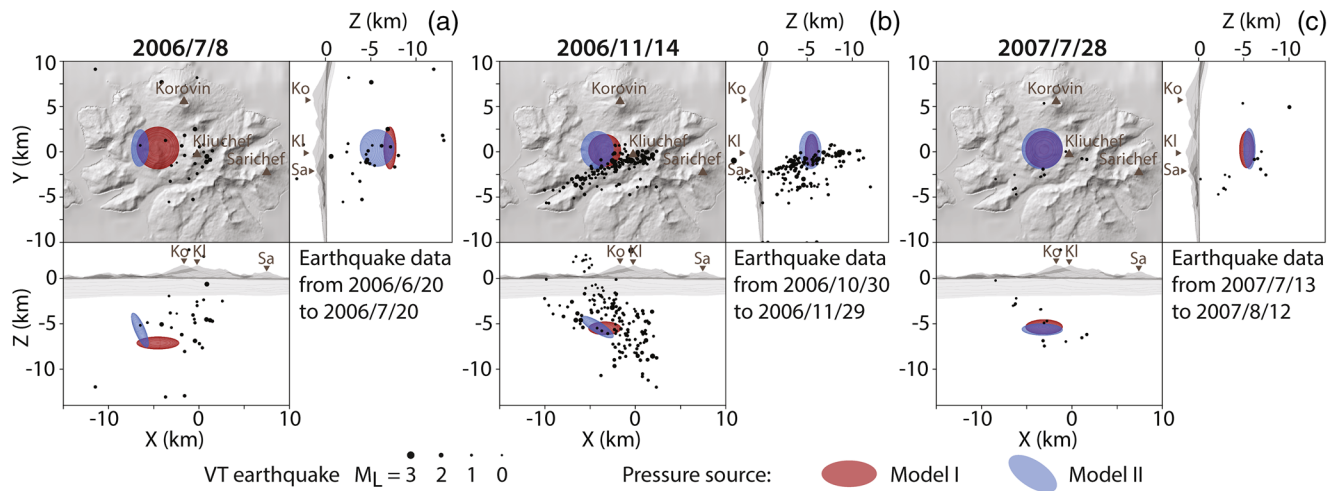


**Figure 6.** The geometry of the pressure sources at three different epochs of the InSAR time series. (a) 2006/7/8, the beginning of the volcanic unrest. (b) 2006/11/14, prior to the eruption. (c) 2007/7/28, 8 months after the eruption. The colored ellipses are the projections of the pressure sources on the XY-, ZY-, and XZ-planes. The red and blue ellipses represent the ensemble averages of Model I and II at the given times. The VT earthquakes within a range of 15 days before and after the InSAR epochs are plotted as black dots. InSAR, interferometric synthetic aperture radar; VT, volcano-tectonic.

surface deformation pattern revealed by the variation of the ratio between lateral and vertical displacements cannot be explained by a stationary pressure source. To exclude the effect of reference selection on deformation patterns, we have also tested a zero-phase reference over the easternmost edge of the island. It produces nearly identical results. Therefore, the derived east-west component and the associated asymmetric characteristic are unlikely due to the selection of the reference point.

Both Model I and II reproduce the general deformation pattern revealed by the InSAR time series (Figures 4 and S4). However, Model II has done a better job to capture the asymmetric deformation pattern in the East-West component during the volcanic unrest (2006/6–2006/11). Specifically, the maximum east-ward motion ( $\sim 40$  mm) is larger than the west-ward motion ( $\sim 10$ – $20$  mm) by at least two times (Figure 4c). After the Korovin eruption, the deformation signal is nearly symmetric (Figure 4g). Therefore, we favor Model II since it fits the asymmetric East-West displacement (Figures 4 and S4). The symmetry variation of the deformation signal cannot be explained by changes in overpressure, size, or even location. The ellipsoid in Model II can rotate freely to generate this asymmetric deformation pattern (Figures 5 and 6). While Model I with a fixed “a” axis can only create symmetric patterns (Figure 6), leading to larger misfits (i.e.,  $L_2$  norm errors) than Model II.

Figure 5 shows the mean values and two times of the standard deviation ( $\sim 95\%$  confidence interval) of the parameter estimations from the two models. Our favorite model (Model II) is a dike-like source centered at 6-km west of Kliuchef (Figure 6a) with a depth of  $\sim 5.8$  km b.s.l. at the beginning of the unrest (2006/6). During the unrest (2006/6–2006/11), the oblate ellipsoid in Model II rotates by  $\sim 30^\circ$  whose plunge evolves from steep to gentle (Figure 5). On July 28, 2007, 8 months after the eruption, both the models indicate the pressure source is an oblate ellipsoid with nearly zero plunges (Figures 5 and 6). The depth of the pressure source of Model II slightly varies from  $\sim 4.8$  to  $\sim 5.8$  km b.s.l., which is comparable to the distribution of the Mogi source depth estimated by a previous study using InSAR pairs (Lu & Dzurisin, 2014). Meanwhile, Model I has a considerable depth variation since translation is the only way for Model I to fit the evolution of displacement pattern. Considering Model II has a better-fit with the data than Model I (Figure 4), we suggest that the pressure source has more likely experienced a  $30^\circ$  rotation rather than a  $>3$ -km vertical translation during the unrest. The overpressure of Model II has a slight change from 7 to 8 MPa during the unrest (Figure 5e).

### 2.5. Implication on Magma Reservoir

By data assimilation with the InSAR time series data, we find that the pressure source may rotate during the volcanic unrest (Figure 6). There are three possible explanations. First, the pressure source migration may

represent dike propagation due to pressurized magma or hydrothermal fluid (e.g., Mastin & Pollard, 1988). However, if it is a dike propagation, the model should show expansion of the pressure source along its long axis rather than rotation. In addition, there is no corresponding VT earthquakes associated with the diking or dike-related brittle failure (Roman & Cashman, 2006). On the contrary, most VT events occurred along the AA fault during the unrest (Figures 1b and 6b). The fault may serve as a pre-existing weak zone to facilitate dike propagation if the fault is perpendicular to the direction of minimum compressive stress. However, the surface deformation pattern is not controlled by the fault (Figure 4), indicating the VT earthquakes along the fault unlikely represent the dike propagation.

The second hypothesis is that the magma or fluid was transported through some pre-existing channels or conduits (e.g., Bonaccorso & Davis, 1999) to create a moving pressure source. However, the pressure source moves laterally with a  $\sim 30^\circ$  rotation, which can hardly be explained by magma or fluid moving along a straight channel or conduit. In addition, even if the fluid is moving through a complicated channel system, we still have difficulty in explaining why the magma does not take advantage of the pre-existing weak zone (i.e., the AA fault). Besides, seismic tremors are usually triggered during fluid migration (e.g., Yamamoto et al., 2002). No evidence shows that the number of tremor events is increasing during the unrest (Figure 2).

We favor the third hypothesis that the pressure source migration is due to the changes in the connectivity of the magma reservoir dominated by a crystal mush. Previous studies by petrology and geochemistry indicated that the Atka volcanic field is supplied by a series of poorly connected but adjacent magma bodies (e.g., Myers et al., 2002). The magma reservoir of Atka is likely to comprise interleaved lenses of melt, partially molten crystal mushes and volatiles (Cashman & Giordano, 2014). The pressure source of Atka may not be a uniform, homogenous magma body. While the pressure source can be an interconnected network with a small proportion of melt or fluid. Melts or volatiles with a fraction as low as 2% is enough to provide the connectivity for a crystal mush to share the same overpressure (Zhu et al., 2011). In Model II, the pressure source rotates  $\sim 30^\circ$ , which can be explained by a diffusion of pore pressure in the crystal mush (e.g., Liao et al., 2018; Sparks & Cashman, 2017). In this scenario, some parts of the crystal mush may be pressurized due to the increment of connectivity driven by deformation or magma processes, while some initially inflated areas may deflate. The overall changes in pressurization status in different regions of the crystal mush may create an effect approximated by a moving pressure source. No significant migration of magma or fluid is needed. The pore pressure diffusion is the dominant process during the deformation of a heterogeneous, poroelastic crystal mush (Liao et al., 2018). In this study, the ellipsoid is an approximation of the pressurized crystal mush, while in reality, the pressurized regions of the magma reservoir can be irregular. However, to determine an irregular pressurized source, we must combine other geophysical observations, such as seismology, magnetotellurics, and gravity.

### 3. Stress and Failure Development

#### 3.1. Failure Criteria

To explain how the VT earthquakes are triggered, we evaluate the stress and failure development associated with the host-rock deformation driven by the pressure source. We calculate the stresses of the Atka host-rock using the pressure source defined by the mean values of the estimated parameters (Figure 5). We use Coulomb and tensile failure criteria to predict whether shear or tensile failure can happen in the host-rock. To quantify the likelihood of failures, we calculate the “stress to failure” (e.g., Zhan & Gregg, 2019), which is defined as the distance of the Mohr circle to the Coulomb or tensile failure envelope (*CF* and *TF* in Figure 7a and 7b). No failure happens when *CF* and *TF* are less than zero. Failure is initiated when *CF* or *TF* becomes positive. The stresses to Coulomb failure (*CF*) and tensile failure (*TF*) are given by

$$CF = \tau - C_0 \cos \phi_i - \sigma_n \sin \phi_i, \quad (6a)$$

and

$$TF = -\sigma_3 - \sigma_T, \quad (6b)$$

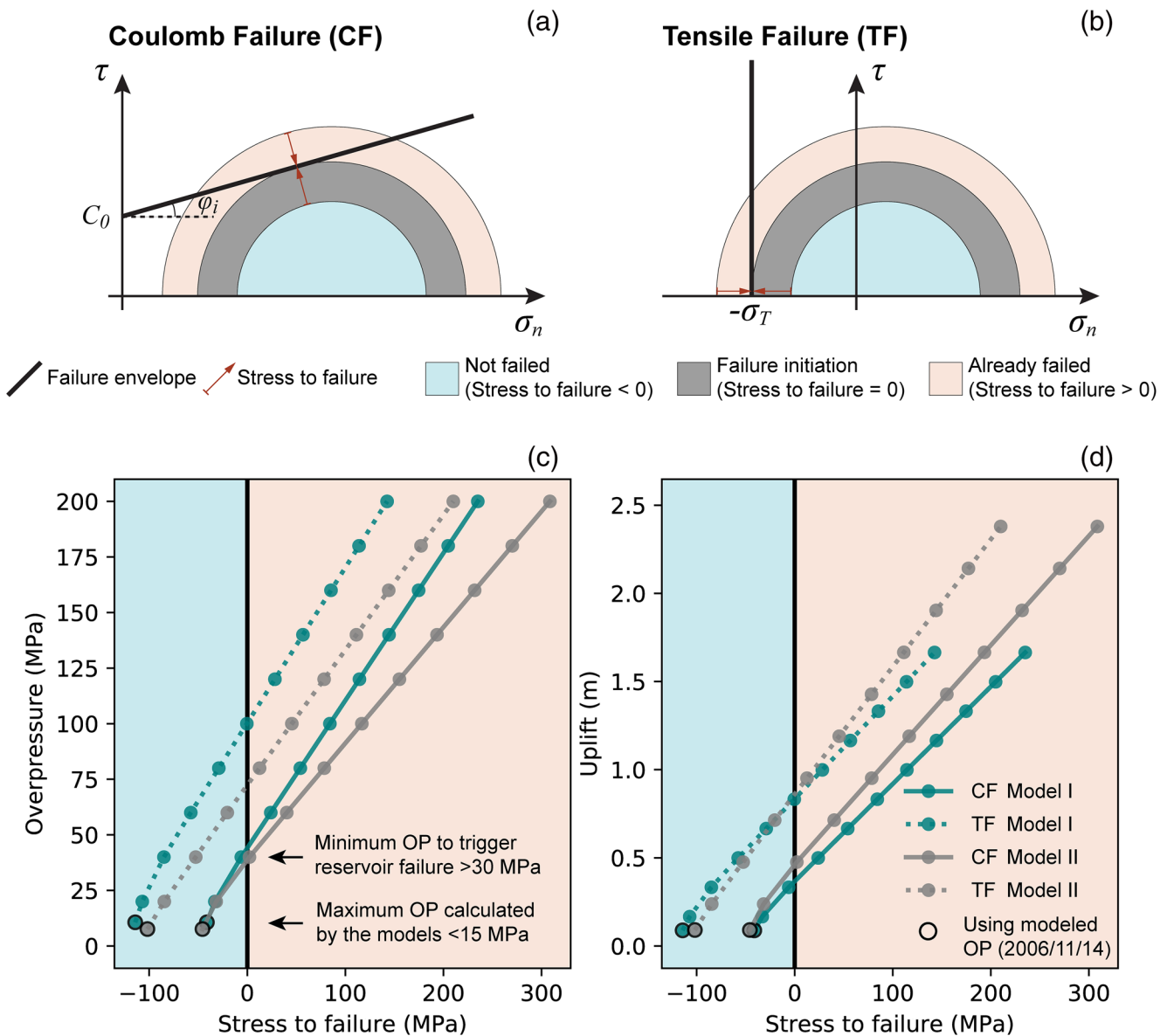


**Figure 7.** The potential of failure occurring at the boundary of the pressure source. (a) and (b) illustrate Coulomb and tensile failure criteria. The possibility of failure is expressed as “stress to failure” (*CF* and *TF*). Mohr circles are defined by normal stress ( $\sigma_n$ ) and shear stress ( $\tau$ ).  $\phi_i$  and  $C_0$  are the internal friction angle and cohesion for Coulomb failure.  $\sigma_T$  is the tensile strength. (c) The “stress to failure” varies with overpressure (c) and surface displacement (d). The colored solid or dotted lines represent the results from different models with different failure types. The black solid lines illustrate the initiation of failure along with the chamber. All plots are calculated by using the geometry of the best-fit pressure sources on November 14, 2006. Extrapolated overpressures are used to test their relationship with the “stress to failure.” Only the markers with black edges show the overpressure (OP) modeled by data assimilation with the InSAR data on November 14, 2006. InSAR, interferometric synthetic aperture radar.

where  $\tau$ ,  $\sigma_n$ , and  $\sigma_3$  are the maximum shear stress, normal stress, and least principal stress (positive for compression). Similar to Zhan et al. (2019), the internal friction angle ( $\phi_i$ ) is  $25^\circ$ , cohesion ( $C_0$ ) is  $E \times 5 \times 10^{-4}$ , and tensile strength ( $\sigma_T$ ) is  $E \times 10^{-4}$ , in which  $E$  is the Young's modulus of the rock.

### 3.2. Overpressure to Generate Host-Rock Failure

The failure calculation shows no failure occurring in the host-rock by 2006/11/14 (Figure 7c and 7d). The overpressures calculated by the EnKF are less than 10 MPa (Figure 5e) to create an 80-mm surface uplift

(Figure 2). At least 30 MPa is needed for any model to generate Coulomb failure along the boundary of the pressure source (Figure 7c). Such an overpressure will create at least 300-mm surface uplift, larger than the observation by at least three times.

Therefore, during the volcanic unrest, the pressurized magma reservoir does not directly cause the failure of the host-rock to trigger the volcano-tectonic earthquakes. First, the overpressure prior to the eruption is much less than the overpressure required to initiate failure in the host-rock. Besides, the widespread host-rock failure does not occur until the overpressure is greater than 100 MPa, which is less likely in a natural system. Even if the magma reservoir can be pressurized to >100 MPa, the failure distribution is not consistent with the VT earthquakes (Figures 6 and S5).

#### 4. Effects of the Pre-existing Weak Zones

An alternative explanation is necessary to link the surface deformation and VT earthquakes in Atka. During the volcanic deformation, some parts of the host-rock may experience dilatancy due to the pressure source, which increases the effective (or connected) porosity of the rock, allowing pore fluid to saturate those dilatant parts. Many examples show that earthquakes can be triggered in areas of positive dilatation, such as Yellowstone (Chang et al., 2007; Taira et al., 2010; Wicks et al., 2006), Copahue (Lundgren et al., 2017), Laguna del Maule (Zhan et al., 2019), and Domuyo (Lundgren et al., 2020) volcanoes.

##### 4.1. Modeling Pre-existing Weak Zone

A previous study at Laguna del Maule shows that a pre-existing weak fault, the Troncoso fault, may serve as a channel for pore fluid (i.e., water or brine) to trigger “hydrofracturing” seismicity during the volcanic deformation (Zhan et al., 2019). By borrowing this idea, we have tested whether the local fault zones (i.e., AA fault and Segum fault) can facilitate pore fluid to trigger the VT earthquakes.

Similar to Zhan et al. (2019), we model the fault zone as a thin vertical slab (~100–1,000 m) embedded in the host-rock (Figure S6). Within the fault zones, Young’s modulus is lower than the surrounding host-rock. The traces of the fault zones are defined after previous studies (Figure 1; e.g., Geist et al., 1987; Singer et al., 1992). We assume that the AA fault is at least 10-km deep and nearly vertical, according to the earthquake distribution (Figure 6b). Since we have less constraints on the geometry of the Segum fault at the Atka Island, we assume it shares the same depth and dipping as the AA fault. In addition, the Segum fault is >7 km away from the deformation center. In the later discussion, we find the volcanic deformation has negligible effects on the Segum fault compared to the AA fault.

To maximize the effects of the fault zones on the stress field, we need the fault zone to be as large and weak as possible, which can be achieved either by increasing the thickness of the fault or by decreasing Young’s modulus. However, as the fault zone becomes thicker or weaker, it can strongly affect the surface deformation pattern. Similar to Zhan et al. (2019), we conduct a series of sensitivity tests to determine the relationships between significance (i.e., thickness and weakness) of the fault zone and its perturbation to the pattern of surface deformation. We find that the faults with either a thickness greater than 500 m, or Young’s modulus lower than 50% of the surrounding host-rock will create a >10% perturbation of surface deformation, which can be observable in the InSAR data (Figure S7). This result is very similar to the study in Laguna del Maule (Zhan et al., 2019), where the magma reservoir is also next to the fault zone. Since the pattern of surface deformation is not affected by any linear, fault-like structure, we argue that the fault zones should not be wider than 500 m and weaker than the surrounding rocks by more than 50%.

##### 4.2. VT-Earthquakes Distribution

In this study, we calculate the volumetric strain evolution within the fault zones (Figures 8 and S8–S10). We compare the change of volumetric strain of the AA fault zone and the distribution of VT earthquakes oc-

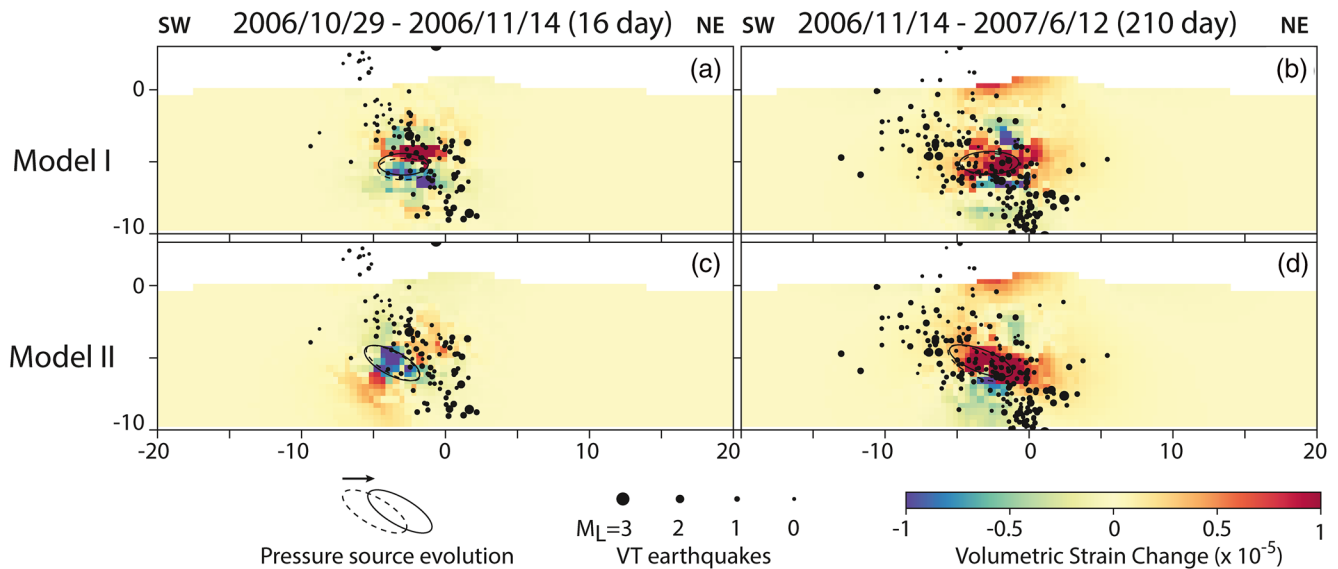


**Figure 8.** Volumetric strain changes within the AA fault during the time periods between different epochs of the InSAR time series. (a) and (c) show the strain changes during two InSAR epochs (2006/10/29 & 2006/11/14) prior to the eruption. (b) and (d) show the strain changes between the time prior to the eruption (2006/11/14) and 6 months after the eruption (2007/6/12) due to the lack of InSAR acquisition. Different rows represent the results from different models. The ellipses with dashed and solid lines are the projections of the pressure sources on the fault plane at the beginning and end of the period. The VT earthquakes which occur within a 2-km-distance to the fault and during the time period are plotted as black dots. AA, Amlia-Amukta; InSAR, interferometric synthetic aperture radar; VT, volcano-tectonic.

curing within a 2-km distance to the AA fault. We find that the VT earthquakes generally favor the regions with volumetric strain increment (Figure 8). This correlation cannot be found before June 2006 (Figure S8 and S9) since the EnKF has not obtained a convincing estimation of the pressure source, as the  $L_2$  norm error is high (Figure 5i).

The pattern of volumetric strain prior to and after the eruption experienced significant changes due to the migration of the pressure source (Figure 8). At the same time, distribution of the VT earthquake also shifted downward (Figure 8), which is consistent with the volumetric strain changes. Between the two models, Model I, using the ellipsoid with a fixed “a” axis, generates a horizontal dilatant zone (Figure 8a and 8b). Model II with a plunging ellipsoid, however, suggests that the area with positive dilatation is extending deep in NE and shallow in SE, which has a larger overlap with the earthquake distribution (Figure 8c and 8d). Compared to Model I, Model II has a better performance not only in reproducing the surface displacement (Figure 4), but also in explaining the earthquake distribution. Although most earthquakes overlap with dilatation of the fault, some earthquakes are located in areas of neutral or negative dilatation. Uncertainties in earthquake hypocenter locations may be one reason for such discrepancies. In addition, our model with a simplified crust structure may overlook some local structures leading to stress localization and earthquake initiation.

In addition, we have calculated volumetric strain evolution of the Segum fault. The magnitude of volumetric strain change is 1–2 orders lower than the AA fault (Figure S10), which is consistent with its much fewer VT events (Figure 1b). The ML3.1 earthquake in 2006/6/15 is probably associated with tectonic processes, for example, the clockwise rotation of the Andreanof Block (Figure 1a).

Alternative to the fault dilatancy model, we have also calculated Coulomb stress change along the AA and Segum fault (Figures S11–S13), in which the sliding friction angle is  $15^\circ$  (Collettini et al., 2009). There is no obvious correlation between distribution of the VT earthquakes and the positive Coulomb stress change (Figures S11–S13). Therefore, we argue that the Coulomb stress change in the fault zone is not the main reason triggering the VT earthquakes.



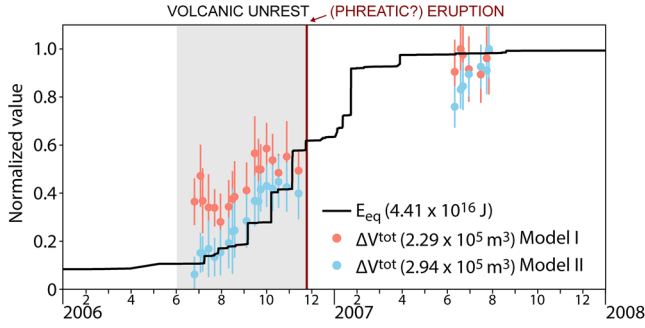


**Figure 9.** Comparison between the VT earthquake energy and volume change of the pre-existing weak zone. Time series of total volume change ( $\Delta V^{tot}$ ) of the AA fault (served as a pre-existing weak zone) calculated by ensemble models are shown as colored dots with error bars. The error bar represents the uncertainty of the ensemble models according to the displacement misfit (i.e.,  $L_2$  norm error). The solid black line shows the accumulated energy releasing ( $E_{eq}$ ) of the VT-earthquakes occurring within a 2-km-distance to the AA fault since 2005/1. In the plots, the time series of  $\Delta V^{tot}$  and  $E_{eq}$  are normalized by their maximum values shown in the legend. AA, Amlia-Amukta; VT, volcano-tectonic.

#### 4.3. Energy Released from the VT-Earthquakes along the Fault

In addition to the spatial correlation between seismicity and fault dilatancy, we also find that there is a temporal correlation between the two processes. We calculate the total volume change ( $\Delta V^{tot}$ ) of the AA fault at each InSAR acquisition time,

$$\Delta V^{tot} = \iiint_{\Omega} \epsilon_v dV, \quad (7)$$

where  $\epsilon_v$  is volumetric strain, and  $V$  is the total volume of the fault.

We find that the total volume change of the AA fault ( $\Delta V^{tot}$ ), and the energy released from the VT earthquakes within a 2-km-distance to the fault ( $E_{eq}$ ) share a similar evolution pattern (Figure 9), which suggests a linear relationship between the energy release rate and the dilatation rate. In particular, Model II fits the observation but Model I, showing the consistency that the model with a capability of reproducing the surface deformation can also explain the distribution and energy release rate of seismicity. This consistency further confirms a linkage between the deformation and seismicity during the volcanic unrest.

The model shows a linear relationship between  $E_{eq}$  and  $\Delta V^{tot}$  (Figure 9) given by

$$E_{eq} \cong \gamma_1 \Delta V^{tot}, \quad (8)$$

where  $\gamma_1$  is a constant which may be controlled by system structures. This linear relationship may be explained by the formation of microfracture (Jaeger et al., 2007). In a dilating fault zone, if we only consider Mode I cracks, the released energy,  $dQ$ , due to the growth of a crack (length =  $2c$ , and thickness =  $t_c$ ; Figure S14) by  $dc$  can be expressed by

$$dQ = \frac{2K_I^2 t_c}{E'} dc \quad (9)$$

where  $E'$  is effective Young's modulus of the pre-existing weak zone.  $K_I$  is the stress intensity factor given by

$$K_I = \sigma_{tip} \sqrt{\pi c}, \quad (10)$$

where  $\sigma_{tip}$  is the stress at the tip of the crack, and  $c$  is the half-length of the crack. Therefore, the energy ( $Q$ ) released by the opening of a single crack with a length of  $c$  is given by

$$Q = \int_0^c \frac{2\pi c \sigma_{tip}^2}{E'} t_c dc = \frac{\pi \sigma_{tip}^2}{E'} t_c c^2, \quad (11)$$

If we assume the crack is an elliptical cylinder, the volume of the crack opened during the fracturing is  $\pi c^2 t_c A_c$ , where  $A_c$  is the aspect ratio of the crack (Figure S14c). We further assume that the effective Young's modulus of the pre-existing weak zone is a constant. Besides, we can use tensile strength of the rock to take place the stress at the crack tip,  $\sigma_{tip}$ , which can also be assumed as constant. If the aspect ratio of the crack  $A_c$  does not change during the crack growth, which means the crack growth is self-similar, the energy released by the earthquake can be approximated by a linear function of the volume change due to opening of the crack.

We calculate the total volume change by integrating the volumetric strain, which is in the elastic regime, while we use fracture mechanics to explain the energy release, representing the inelastic behavior of rock (Jaeger et al., 2007). Although these two processes are based on two different theorems, we argue that the

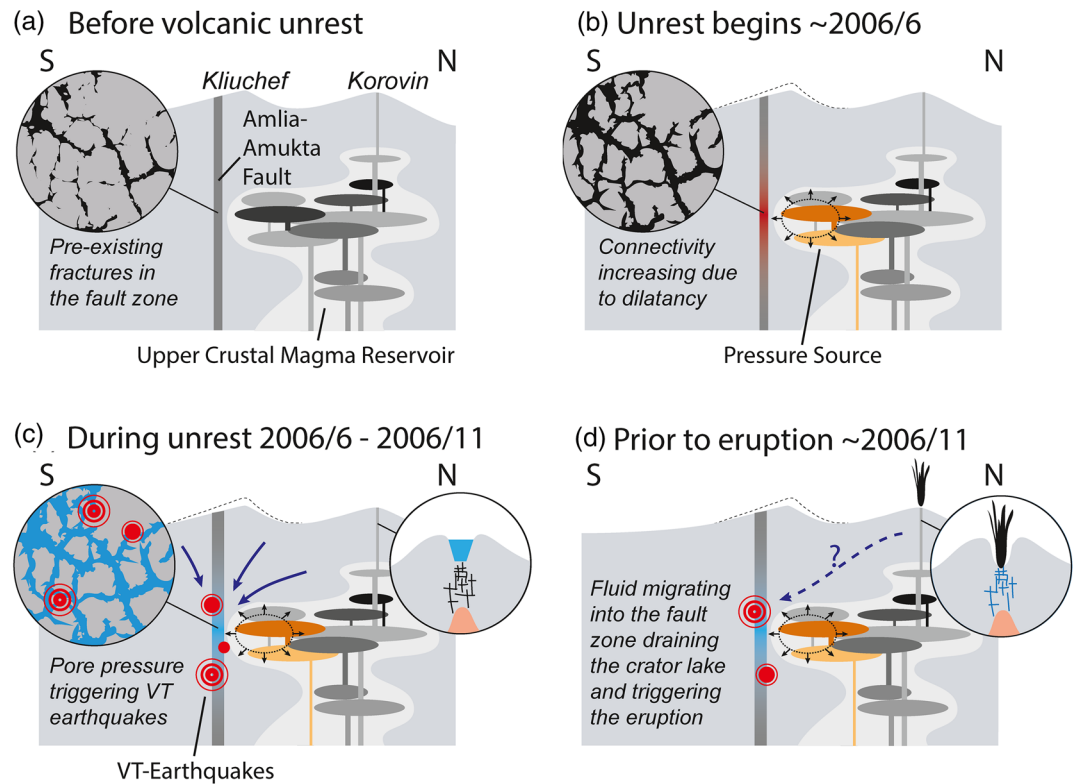


**Figure 10.** Cartoons illustrating the interaction between the magma reservoir and AA fault during the volcanic unrest and its implication to the eruption on November 25, 2006. (a) The Atka volcanic center has developed a complex upper crustal magma reservoir generating a series of Quaternary volcanic activities (Myers et al., 2002). The magma reservoir is likely composed of a series of poorly connected magma body and crystal mush (modified after Myers et al., 2002). The AA fault is a pre-existing weak zone with fractures and pores. (b) The volcanic unrest began around June 2006. A pressure source due to possible melt/fluid injection or magma differentiation might generate surface deformation and the dilatancy in some parts of the AA fault, causing connectivity of the fault to increase. (c) The fluid (e.g., water or brine) was allowed to migrate into the fault zone where the permeability is increased. Increased pore pressure might trigger the VT earthquakes around the AA fault zone. (d) Once the fluid migrated into the fault zone, the crater lake at Korovin might be discharged (Neal et al., 2008). A phreatic eruption might be triggered due to the drop of the water table. AA, Amlia-Amukta; VT, volcano-tectonic.

inelastic dilatancy of a pre-existing weak zone at the microscale (i.e., fracture opening and growth) can be approximated by the elastic expansion at the macroscale if the pre-existing weakness is homogenous within the weak zone. In summary, the correlation between the VT earthquake energy and the fault dilatation suggests that the seismicity in Atka during the unrest was likely triggered by dilatancy-related “hydrofracturing” processes, similar to the Yellowstone (Chang et al., 2007; Taira et al., 2010; Wicks et al., 2006), Copahue (Lundgren et al., 2017), Laguna del Maule (Zhan et al., 2019), and Domuyo (Lundgren et al., 2020) volcanoes. However, future studies are necessary to understand the details in fracturing processes during volcanic unrest.

## 5. 2006–2007 Atka Volcanic Unrest and the Eruption at Korovin

By integrating the surface deformation modeling, stress and strain calculation, and seismicity, we suggest that the surface deformation and seismicity observed during the volcanic unrest are closely linked to each other. In particular, the pressure source may be driven by an injection of magma/fluid, or differentiation of a long-existent, complex magma system (Myers et al., 2002; Figure 10a). Deformation of the mushy magma reservoir may change the matrix’s connectivity, causing the migration of the pressure source (Figure 6). At the same time, the pressure source may trigger opening and growth of the fractures within the AA fault

(Figure 10b), leading to an increment in conductivity or permeability of the fault. Pore fluids may inject into the dilatant parts of the fault, decreasing the effective stress, and triggering the brittle failures (i.e., the VT earthquakes; Figure 10c).

The dilatant fault may serve as a sink (on the order of  $10^5 \text{ m}^3$ ) for the groundwater at Atka, similar to the process proposed at Kilauea (Hurwitz & Johnston, 2003) and Mayon (Albano et al., 2001) volcanoes. Considering that there is an active hydrothermal system  $\sim 2\text{--}3 \text{ km}$  beneath Atka revealed by a previous InSAR study (Lu & Dzurisin, 2014) and the geological records (McGimsey et al., 2007, 2011; Neal et al., 2008), the hydrothermal system at Korovin may connect to the Atka fault system through this shallow “hydrofluid zone” (Lu & Dzurisin, 2014). The water table at Korovin may drop due to water discharge (Figure 10d), which is consistent with the lake drainage event occurring between September and October 2006 (Neal et al., 2008). The local subsidence near the Korovin vent (Figure 2) may also be associated with the drainage of the crater lake. Finally, drop in the water table may have triggered the phreatic eruption of Korovin. However, there is no direct evidence showing that the hydrothermal system at the Korovin volcano is connected to the fault system near the Atka volcanic center. Our model does not exclude the possibility that the discharge of the crater lake at Korovin is due to a local variation of hydrostatic head, which coincided with the unrest at the Atka volcanic center.

This study is another example to illustrate that pre-existing weak zones and pore fluids may play important roles in driving volcanic unrest and triggering eruptions, especially for a volcano with a shallow hydrothermal system (e.g., Dzurisin et al., 2012). The “hydrofracturing” process is sensitive to physical condition changes of a volcanic system, which provides critical information for forecasting eruptions.

## 6. Conclusions

Constrained by the InSAR timeseries data, our models indicate that a NE-tilted, oblate, ellipsoidal pressure source may produce the rapid uplift ( $\sim 80 \text{ mm/yr}$ ) observed during the 2006–2007 volcanic unrest of the Atka volcanic center. Model results further indicate that the pressure source rotated from steep to gentle dipping from the period of June to November 2006, creating an asymmetric deformation pattern. Conceptually, migration of the pressure source may imply changes in connectivity and, therefore, pressure distribution in a crystal mush potentially driven by magma injection or differentiation. In this scenario, the overall overpressure may remain constant, while the distribution of overpressurized crystal mush may change as expressed in the surface deformation. To investigate the VT earthquakes at the Atka volcanic center, stress and failure are modeled within the host-rock driven by the pressure source. However, without pore pressure, no modeled failure is observed due to the overpressure derived from the surface deformation modeling. The source overpressure must exceed the best-fit model overpressure by at least three times to initiate the brittle failure needed to explain the observed seismicity during the unrest, which is unlikely. Alternatively, we test the hypothesis that a pre-existing weak zone, the Amulia-Amukta fault, may serve as a channel to allow pore fluid injection to trigger the seismicity. The calculated volume change within the fault zone suggests that the seismicity distribution is consistent with the dilatant regions of the fault. In addition, the energy released from the observed VT earthquakes along the fault is proportional to the volume increment of the fault during the unrest. VT earthquakes may be triggered by pore fluid injections, which are associated with permeability increment due to the opening of the fractures within the fault during the uplift. Therefore, we propose a possible model for the phreatic eruption of the Korovin volcano. Water discharge at Atka, on the order of  $10^5 \text{ m}^3$ , may have occurred due to the injection of water into the dilatated regions of the pre-existing weak zone. Subsequently, the drop of the water table may have caused the discharge of the crater lake at Korovin by October 19, 2006, and finally triggered the phreatic eruption of the Korovin volcano on November 25, 2006.

## Data Availability Statement

All data and modeling results are available at “Figshare” ([10.6084/m9.figshare.13388783](https://doi.org/10.6084/m9.figshare.13388783)).

## Acknowledgments

The authors are grateful for helpful discussions with J. Power, B. Singer, C. Lundstrom, L. Liu, S. Marshak, D. Roman, H. Le Mével, D. Peng, J. Albright, H. Cabaniss, R. Goldman, and the UIUC Geodynamics Group. The authors would also like to thank F. Delgado, A. Hooper, S. Parman, and one anonymous reviewer for their comments that significantly improved our manuscript. The development of a high-performance computing data assimilation framework for forecasting volcanic unrest is supported by grants from NASA (19-EARTH19R-0104 – Zhan, 18-ESI18-0002 – Gregg/Lu) and the National Science Foundation (OCE 1834843, EAR 1752477 – Gregg).

## References

- Acocella, V. (2014). Structural control on magmatism along divergent and convergent plate boundaries: Overview, model, problems. *Earth-Science Reviews*, 136(Supplement C), 226–288. <https://doi.org/10.1016/j.earscirev.2014.05.006>
- Albano, S. E., Sandoval, T., & Toledo, R. (2001). *Groundwater at Mayon, volcano*. AGU Fall Meeting 2001. V42B1017.
- Albright, J. A., Gregg, P. M., Lu, Z., & Freymueller, J. T. (2019). Hindcasting magma reservoir stability preceding the 2008 eruption of Okmok, Alaska. *Geophysical Research Letters*, 46(15), 8801–8808. <https://doi.org/10.1029/2019GL083395>
- Anderson, K., & Segall, P. (2013). Bayesian inversion of data from effusive volcanic eruptions using physics-based models: Application to Mount St. Helens 2004–2008. *Journal of Geophysical Research-Solid Earth*, 118(5), 2017–2037. <https://doi.org/10.1002/jgrb.50169>
- Bato, M. G., Pinel, V., & Yan, Y. (2017). Assimilation of deformation data for eruption forecasting: Potentiality assessment based on synthetic cases. *Frontiers in Earth Science*, 5, 48. <https://doi.org/10.3389/feart.2017.00048>
- Berardino, P., Fornaro, G., Lanari, R., & Sansosti, E. (2002). A new algorithm for surface deformation monitoring based on small baseline differential SAR interferograms. *IEEE Transactions on Geoscience and Remote Sensing*, 40(11), 2375–2383. <https://doi.org/10.1109/TGRS.2002.803792>
- Bonaccorso, A., & Davis, P. M. (1999). Models of ground deformation from vertical volcanic conduits with application to eruptions of Mount St. Helens and Mount Etna. *Journal of Geophysical Research*, 104(B5), 10531–10542. <https://doi.org/10.1029/1999JB900054>
- Cashman, K. V., & Giordano, G. (2014). Calderas and magma reservoirs. *Journal of Volcanology and Geothermal Research*, 288, 28–45. <https://doi.org/10.1016/j.jvolgeores.2014.09.007>
- Chang, W.-L., Smith, R. B., Wicks, C., Farrell, J. M., & Puskas, C. M. (2007). Accelerated Uplift and Magmatic Intrusion of the Yellowstone Caldera, 2004 to 2006. *Science*, 318(5852), 952–956. <https://doi.org/10.1126/science.1146842>
- Charco, M., & Galán del Sastre, P. (2014). Efficient inversion of three-dimensional finite element models of volcano deformation. *Geophysical Journal International*, 196(3), 1441–1454. <https://doi.org/10.1093/gji/ggt490>
- Ciccotti, M., & Mulargia, F. (2004). Differences between static and dynamic elastic moduli of a typical seismogenic rock. *Geophysical Journal International*, 157(1), 474–477. <https://doi.org/10.1111/j.1365-246X.2004.02213.x>
- Collettini, C., Niemeijer, A., Viti, C., & Marone, C. (2009). Fault zone fabric and fault weakness. *Nature*, 462(7275), 907–910. <https://doi.org/10.1038/nature08585>
- Currenti, G., Del Negro, C., & Ganci, G. (2007). Modeling of ground deformation and gravity fields using finite element method: An application to Etna volcano. *Geophysical Journal International*, 169(2), 775–786. <https://doi.org/10.1111/j.1365-246X.2007.03380.x>
- Currie, C. A., & Hyndman, R. D. (2006). The thermal structure of subduction zone back arcs. *Journal of Geophysical Research*, 111(B8). <https://doi.org/10.1029/2005JB004024>
- Del Negro, C., Currenti, G., & Scandura, D. (2009). Temperature-dependent viscoelastic modeling of ground deformation: Application to Etna volcano during the 1993–1997 inflation period. *Physics of the Earth and Planetary Interiors*, 172(3), 299–309. <https://doi.org/10.1016/j.pepi.2008.10.019>
- Dzurisin, D., Wicks, C. W., & Poland, M. P. (2012). *History of Surface Displacements at the Yellowstone Caldera, Wyoming, from Leveling Surveys and InSAR Observations, 1923–2008*. Reston, VA: U.S. Geological Survey. <https://doi.org/10.3133/pp1788>
- Ebmeier, S. K., Andrews, B. J., Araya, M. C., Arnold, D. W. D., Biggs, J., Cooper, C., et al. (2018). Synthesis of global satellite observations of magmatic and volcanic deformation: Implications for volcano monitoring & the lateral extent of magmatic domains. *Journal of Applied Volcanology*, 7(1). <https://doi.org/10.1186/s13617-018-0071-3>
- Evensen, G. (2003). The ensemble Kalman filter: Theoretical formulation and practical implementation. *Ocean Dynamics*, 53(4), 343–367. <https://doi.org/10.1007/s10236-003-0036-9>
- Fliedner, M. M., & Klemperer, S. L. (1999). Structure of an island-arc: Wide-angle seismic studies in the eastern Aleutian Islands, Alaska. *Journal of Geophysical Research*, 104(B5), 10667–10694. <https://doi.org/10.1029/98JB01499>
- Fournier, N., & Chardot, L. (2012). Understanding volcano hydrothermal unrest from geodetic observations: Insights from numerical modeling and application to White Island volcano, New Zealand. *Journal of Geophysical Research*, 117(B11). <https://doi.org/10.1029/2012JB009469>
- Geist, E. L., Childs, J. R., & Scholl, D. W. (1987). Evolution and petroleum geology of Amlia and Amukta intra-arc summit basins, Aleutian Ridge. *Marine and Petroleum Geology*, 4(4), 334–352. [https://doi.org/10.1016/0264-8172\(87\)90011-0](https://doi.org/10.1016/0264-8172(87)90011-0)
- Gerbault, M. (2012). Pressure conditions for shear and tensile failure around a circular magma chamber; insight from elasto-plastic modeling. *Geological Society, London, Special Publications*, 367(1), 111–130. <https://doi.org/10.1144/SP367.8>
- Gregg, P. M., de Silva, S. L., & Grosfils, E. B. (2013). Thermomechanics of shallow magma chamber pressurization: Implications for the assessment of ground deformation data at active volcanoes. *Earth and Planetary Science Letters*, 384, 100–108. <https://doi.org/10.1016/j.epsl.2013.09.040>
- Gregg, P. M., de Silva, S. L., Grosfils, E. B., & Parmigiani, J. P. (2012). Catastrophic caldera-forming eruptions: Thermomechanics and implications for eruption triggering and maximum caldera dimensions on Earth. *Journal of Volcanology and Geothermal Research*, 241–242, 1–12. <https://doi.org/10.1016/j.jvolgeores.2012.06.009>
- Gregg, P. M., & Pettijohn, J. C. (2016). A multi-data stream assimilation framework for the assessment of volcanic unrest. *Journal of Volcanology and Geothermal Research*, 309, 63–77. <https://doi.org/10.1016/j.jvolgeores.2015.11.008>
- Grosfils, E. B. (2007). Magma reservoir failure on the terrestrial planets: Assessing the importance of gravitational loading in simple elastic models. *Journal of Volcanology and Geothermal Research*, 166(2), 47–75. <https://doi.org/10.1016/j.jvolgeores.2007.06.007>
- Gutenberg, B. (1956). The energy of earthquakes. *Quarterly Journal of the Geological Society*, 112(1–4), 1–14. <https://doi.org/10.1144/GSL.JGS.1956.112.01-04.02>
- Hickey, J., Gottsmann, J., & Mothes, P. (2015). Estimating volcanic deformation source parameters with a finite element inversion: The 2001–2002 unrest at Cotopaxi volcano, Ecuador. *Journal of Geophysical Research: Solid Earth*, 120(3), 1473–1486. <https://doi.org/10.1002/2014JB011731>
- Hooper, A. (2008). A multi-temporal InSAR method incorporating both persistent scatterer and small baseline approaches. *Geophysical Research Letters*, 35, L16302. <https://doi.org/10.1029/2008GL034654>
- Hurwitz, S., & Johnston, M. J. S. (2003). Groundwater level changes in a deep well in response to a magma intrusion event on Kilauea Volcano, Hawai'i. *Geophysical Research Letters*, 30(22), 2173. <https://doi.org/10.1029/2003GL018676>
- Jaeger, J. C., Cook, N. G. W., & Zimmerman, R. W. (2007). *Fundamentals of rock mechanics*. (4th ed.). Malden, MA: Blackwell Pub.
- Kim, J. W., & Lu, Z. (2018). Association between localized geohazards in West Texas and human activities, recognized by Sentinel-1A/B satellite radar imagery. *Scientific Reports*, 8, 4727. <https://doi.org/10.1038/s41598-018-23143-6>



- Le Mével, H., Gregg, P. M., & Feigl, K. L. (2016). Magma injection into a long-lived reservoir to explain geodetically measured uplift: Application to the 2007–2014 unrest episode at Laguna del Maule volcanic field, Chile. *Journal of Geophysical Research: Solid Earth*, 121(8), 2016JB013066. <https://doi.org/10.1002/2016JB013066>
- Liao, Y., Soule, S. A., & Jones, M. (2018). On the mechanical effects of poroelastic crystal mush in classical magma chamber models. *Journal of Geophysical Research: Solid Earth*, 123(11), 9376–9406. <https://doi.org/10.1029/2018JB015985>
- Lu, Z., & Dzurisin, D. (2014). *InSAR imaging of aleutian volcanoes*. Berlin, Heidelberg: Springer Berlin Heidelberg. Retrieved from <http://link.springer.com/10.1007/978-3-642-00348-6>
- Lu, Z., Jung, H. S., Zhang, L., Lee, W. J., Lee, C. W., & Dzurisin, D. (2012). In X. Yang, & J. Li (Eds.), *DEM generation from satellite InSAR: Advanced in mapping from aerospace imagery: Techniques and applications*. (pp. 119–144), CRC Press.
- Lu, Z., Mann, D., Freymueller, J. T., & Meyer, D. J. (2000). Synthetic aperture radar interferometry of Okmok volcano, Alaska: Radar observations. *Journal of Geophysical Research*, 105(B5), 10791–10806. <https://doi.org/10.1029/2000JB000034>
- Lundgren, P., Girona, T., Bato, M. G., Realmuto, V. J., Samsonov, S., Cardona, C., et al. (2020). The dynamics of large silicic systems from satellite remote sensing observations: The intriguing case of Domuyo volcano, Argentina. *Scientific Reports*, 10(1), 11642. <https://doi.org/10.1038/s41598-020-67982-8>
- Lundgren, P., Nikkhoo, M., Samsonov, S. V., Milillo, P., Gil-Cruz, F., & Lazo, J. (2017). Source model for the Copahue volcano magma plumbing system constrained by InSAR surface deformation observations. *Journal of Geophysical Research: Solid Earth*, 122(7), 5729–5747. <https://doi.org/10.1002/2017JB014368>
- MacQueen, P., Delgado, F., Reath, K., Pritchard, M. E., Bagnardi, M., Milillo, P., et al. (2020). Volcano-tectonic interactions at Sabancaya Volcano, Peru: Eruptions, magmatic inflation, moderate earthquakes, and fault creep. *Journal of Geophysical Research: Solid Earth*, 125(5), e2019JB019281. <https://doi.org/10.1029/2019JB019281>
- Manconi, A., Walter, T. R., Manzo, M., Zeni, G., Tizzani, P., Sansosti, E., & Lanari, R. (2010). On the effects of 3-D mechanical heterogeneities at Campi Flegrei caldera, southern Italy. *Journal of Geophysical Research*, 115(B8), B08405. <https://doi.org/10.1029/2009JB007099>
- Marsh, B. D. (1990). *Atka, central Aleutian islands*. Volcanoes of North America, 29–31.
- Massonnet, D., & Feigl, K. L. (1995). Discrimination of geophysical phenomena in satellite radar interferograms. *Geophysical Research Letters*, 22(12), 1537–1540. <https://doi.org/10.1029/95GL00711>
- Masterlark, T. (2007). Magma intrusion and deformation predictions: Sensitivities to the Mogi assumptions. *Journal of Geophysical Research*, 112(B6). <https://doi.org/10.1029/2006JB004860>
- Mastin, L. G., & Pollard, D. D. (1988). Surface deformation and shallow dike intrusion processes at inyo craters, Long Valley, California. *Journal of Geophysical Research*, 93(B11), 13221–13235. [https://doi.org/10.1029/JB093iB11p13221@10.1002/\(ISSN\)2169-9356](https://doi.org/10.1029/JB093iB11p13221@10.1002/(ISSN)2169-9356). LVCCAL1
- McGimsey, R. G., Neal, C. A., Dixon, J. P., Malik, N., & Chibisova, M. (2011). *2007 volcanic activity in Alaska, Kamchatka, and the Kurile islands: Summary of events and response of the Alaska volcano observatory (No. 2010–5242)*. U.S. Geological Survey. Retrieved from <https://pubs.usgs.gov/sir/2010/5242/>
- McGimsey, R. G., Neal, C. A., Dixon, J. P., & Ushakov, S. (2007). *2005 volcanic Activity in Alaska, Kamchatka, and the Kurile islands: Summary of Events and Response of the Alaska volcano observatory (No. 2007–5269)*. U.S. Geological Survey. Retrieved from <https://pubs.usgs.gov/sir/2007/5269/>
- McTigue, D. F. (1987). Elastic stress and deformation near a finite spherical magma body: Resolution of the point source paradox. *Journal of Geophysical Research*, 92(B12), 12931. <http://dx.doi.org/10.1029/jb092ib12p12931>
- McTigue, D. F., & Mei, C. C. (1981). Gravity-induced stresses near topography of small slope. *Journal of Geophysical Research*, 86(B10), 9268–9278. <https://doi.org/10.1029/JB086B10p09268>
- Mogi, K. (1958). Relations between the Eruptions of Various Volcanoes and the Deformations of the Ground Surfaces Around Them. *Bulletin of the Earthquake Research Institute*, University of Tokyo, 36, 99–134.
- Moran, S. C., Newhall, C., & Roman, D. C. (2011). Failed magmatic eruptions: Late-stage cessation of magma ascent. *Bulletin of Volcanology*, 73(2), 115–122. <https://doi.org/10.1007/s00445-010-0444-x>
- Myers, J. D., Marsh, B. D., Frost, C. D., & Linton, J. A. (2002). Petrologic constraints on the spatial distribution of crustal magma chambers, Atka Volcanic Center, central Aleutian arc. *Contributions to Mineralogy and Petrology*, 143(5), 567–586. <https://doi.org/10.1007/s00410-002-0356-7>
- Neal, C. A., McGimsey, R. G., Dixon, J. P., Manevich, A., & Rybin, A. (2008). *2006 volcanic Activity in Alaska, Kamchatka, and the Kurile islands: Summary of Events and Response of the Alaska volcano observatory (USGS numbered series No. 2008–5214)*. U.S. Geological Survey. Retrieved from <http://pubs.er.usgs.gov/publication/sir20085214>
- Phillipson, G., Sobrado, R., & Gottsmann, J. (2013). Global volcanic unrest in the 21st century: An analysis of the first decade. *Journal of Volcanology and Geothermal Research*, 264, 183–196. <https://doi.org/10.1016/j.jvolgeores.2013.08.004>
- Power, J. A., Friberg, P. A., Haney, M. M., Parker, T., Stihler, S. D., & Dixon, J. P. (2019). *A unified catalog of earthquake hypocenters and magnitudes at volcanoes in Alaska—1989 to 2018 (USGS Numbered Series No. 2019–5037)*. Reston, VA: U.S. Geological Survey. Retrieved from <http://pubs.er.usgs.gov/publication/sir20195037>
- Roman, D. C., & Cashman, K. V. (2006). The origin of volcano-tectonic earthquake swarms. *Geology*, 34(6). <https://doi.org/10.1130/G22269.1>
- Roman, D. C., & Cashman, K. V. (2018). Top-down precursory volcanic seismicity: Implications for ‘stealth’ magma ascent and long-term eruption forecasting. *Frontiers in Earth Science*, 6. <https://doi.org/10.3389/feart.2018.00124>
- Ryan, W. B. F., Carbotte, S. M., Coplan, J. O., O’Hara, S., Melkonian, A., Arko, R., et al. (2009). Global multi-resolution topography synthesis. *Geochemistry, Geophysics, Geosystems*, 10(3). <https://doi.org/10.1029/2008GC002332>
- Samsonov, S. (2018). *High-performance system for monitoring ground deformation from RCM SAR data*. Washington DC: AGU 2018 Fall Meeting, December.1014
- Samsonov, S. V., & d’Oreye, N. (2017). Multidimensional small baseline subset (msbas) for two-dimensional deformation analysis: Case study Mexico City. *Canadian Journal of Remote Sensing*, 43(4), 318–329. <https://doi.org/10.1080/07038992.2017.1344926>
- Samsonov, S., d’Oreye, N., & Smets, B. (2013). Ground deformation associated with post-mining activity at the French–German border revealed by novel InSAR time series method. *International Journal of Applied Earth Observation and Geoinformation*, 23, 142–154. <https://doi.org/10.1016/j.jag.2012.12.008>
- Segall, P. (2013). Volcano deformation and eruption forecasting. *Geological Society, London, Special Publications*, 380(1), 85–106. <https://doi.org/10.1144/SP380.4>
- Singer, B. S., Myers, J. D., & Frost, C. D. (1992). Mid-Pleistocene lavas from the Seguam volcanic center, central Aleutian arc: Closed-system fractional crystallization of a basalt to rhyodacite eruptive suite. *Contributions to Mineralogy and Petrology*, 110(1), 87–112. <https://doi.org/10.1007/BF00310884>



- Smith, R., Sammonds, P. R., & Kilburn, C. R. J. (2009). Fracturing of volcanic systems: Experimental insights into pre-eruptive conditions. *Earth and Planetary Science Letters*, 280(1–4), 211–219. <https://doi.org/10.1016/j.epsl.2009.01.032>
- Sparks, R. S. J. (2003). Forecasting volcanic eruptions. *Earth and Planetary Science Letters*, 210(1–2), 1–15. [https://doi.org/10.1016/S0012-821X\(03\)00124-9](https://doi.org/10.1016/S0012-821X(03)00124-9)
- Sparks, R. S. J., Biggs, J., & Neuberg, J. W. (2012). Monitoring Volcanoes. *Science*, 335(6074), 1310–1311. <https://doi.org/10.1126/science.1219485>
- Sparks, R. S. J., & Cashman, K. V. (2017). Dynamic magma systems: Implications for forecasting volcanic activity. *Elements*, 13(1), 35–40. <https://doi.org/10.2113/gselements.13.1.35>
- Starzec, P. (1999). Dynamic elastic properties of crystalline rocks from south-west Sweden. *International Journal of Rock Mechanics and Mining Sciences*, 36(2), 265–272. [https://doi.org/10.1016/S0148-9062\(99\)00011-X](https://doi.org/10.1016/S0148-9062(99)00011-X)
- Taira, T., Smith, R. B., & Chang, W.-L. (2010). Seismic evidence for dilatational source deformations accompanying the 2004–2008 Yellowstone accelerated uplift episode. *Journal of Geophysical Research*, 115(B2). <https://doi.org/10.1029/2008JB006281>
- Wicks, C. W., Thatcher, W., Dzurisin, D., & Svarc, J. (2006). Uplift, thermal unrest and magma intrusion at Yellowstone caldera. *Nature*, 440(7080), 72–75. <https://doi.org/10.1038/nature04507>
- Yamamoto, M., Kawakatsu, H., Yomogida, K., & Koyama, J. (2002). Long-period (12 sec) volcanic tremor observed at Usu 2000 eruption: Seismological detection of a deep magma plumbing system. *Geophysical Research Letters*, 29(9), 43–1. <https://doi.org/10.1029/2001GL013996>
- Yang, X.-M., Davis, P. M., & Dieterich, J. H. (1988). Deformation from inflation of a dipping finite prolate spheroid in an elastic half-space as a model for volcanic stressing. *Journal of Geophysical Research*, 93(B5), 4249–4257. <https://doi.org/10.1029/JB093iB05p04249>
- Zhan, Y., & Gregg, P. M. (2017). Data assimilation strategies for volcano geodesy. *Journal of Volcanology and Geothermal Research*, 344(Supplement C), 13–25. <https://doi.org/10.1016/j.jvolgeores.2017.02.015>
- Zhan, Y., & Gregg, P. M. (2019). How accurately can we model magma reservoir failure with uncertainties in host-rock rheology? *Journal of Geophysical Research: Solid Earth*, 124(8), 8030–8042. <https://doi.org/10.1029/2019JB018178>
- Zhan, Y., Gregg, P. M., Mével, H. L., Miller, C. A., & Cardona, C. (2019). Integrating reservoir dynamics, crustal stress, and geophysical observations of the laguna del maule magmatic system by FEM models and data assimilation. *Journal of Geophysical Research: Solid Earth*, 124(12), 13547–13562. <https://doi.org/10.1029/2019JB018681>
- Zhu, W., Gaetani, G. A., Fosseis, F., Montesi, L. G. J., & De Carlo, F. (2011). Microtomography of partially molten rocks: Three-dimensional melt distribution in mantle peridotite. *Science*, 332(6025), 88–91. <https://doi.org/10.1126/science.1202221>